JOURNAL OF PROPULSION AND POWER
Vol. 26, No. 6, November–December 2010

Hybrid Reynolds-Averaged Navier–Stokes/Kinetic-Eddy Simulation of Stall Inception in Axial Compressors

Mina Zaki,* Lakshmi N. Sankar,† and Suresh Menon‡
Georgia Institute of Technology, Atlanta, Georgia 30332-0150

DOI: 10.2514/1.50195

A hybrid Reynolds-averaged Navier–Stokes/kinetic-eddy simulation turbulence model is used for the stall predictions in a transonic axial compressor stage. This hybrid Reynolds-averaged Navier–Stokes/kinetic-eddy simulation model solves Menter's k-ω–shear-stress-transport model near walls and switches to the kinetic-eddy simulation model away from walls. The kinetic-eddy simulation model solves directly for local turbulent kinetic energy and local turbulent length scales, thus alleviating the grid spacing dependency found in other detached-eddy simulation and hybrid Reynolds-averaged Navier–Stokes/large-eddy simulation models. The current methodology is used in the prediction of the performance map and the stall inception for the NASA stage 35 compressor configuration as a representative of a modern compressor stage. The present approach is found to satisfactorily predict the onset of stall. It is found that the rotor blade-tip leakage vortex and its interaction with the shock wave is the main reason behind the stall inception in this compressor stage.

I. Introduction

AXIAL compressors have a wide variety of aerodynamic applications. They are one of the most important components in modern aeroengines. The flow through axial compressors is very complicated; it is inherently three dimensional and unsteady due to the relative motion between the successive blade rows and the viscous effect associated with each row. The flow is also transonic in nature where regions of subsonic and supersonic flow coexist. Supersonic flow usually appears near the rotor-tip leading edge where the highest rotational velocity is combined with the flow axial velocity, and the flow relative Mach number exceeds 1.0. This leads to the formation of a system of shock waves and shock boundary-layer interactions.

This complicated nature of the flowfield coupled with highly loaded blades makes it critical to maintain a suitable operating range. Compressors' useful range of operation is limited at both very high mass flow rates and very low mass flow rates. At high mass flow rates, the compressor operation is limited by the formation of shock waves and the flow through the compressor chokes, while at low mass flow rates, the compressor operation is limited by the occurrence of certain aerodynamic instabilities. Compressor aerodynamic instabilities are major aspects in compressor design and performance prediction. There are two major aerodynamic instabilities that occur in compressors, known as stall and surge. Compressor stall occurs first, then it grows with time, causing surge, which are more severe and dangerous flow instability phenomena than stall.

A typical performance map for the compression system is shown in Fig. 1, where the rotor revolutions per minute (RPM) are varied, the horizontal axis represents the mass flow rate through the compressor, and the vertical axis represents the total pressure rise across the compressor. The dashed line on this plot represents the stall/surge line. But stall and surge could still occur on the right side of the stall/surge line, which is why the operating points are shifted to another broken line called the surge avoidance line. The closer the operating point is to the stall/surge line, the greater the benefit of increased pressure ratio, but the risk of stall or surge also increases. Compressor designers strive to extend the operating range of the compression systems by using different active or passive flow control techniques. To do that, we need to accurately predict the onset of the stall and understand the physics behind it. Experimental and computational methods are two approaches for investigating these adverse aerodynamic phenomena. In this study, computational investigations are made to study the inception of stall in a transonic compressor stage and to understand the relevant flow mechanisms behind it.

II. Background

Compressor stall is a two-dimensional (2-D) unsteady local phenomenon in which the flow is no longer uniform in the azimuthal direction. The average mass flow through the compressor during rotating stall is steady, but the flow has a circumferentially nonuniform mass deficit [1,2]. Many efforts have been made on the revealing of the stall inception mechanism. It is well known that there are two distinctive routes to stall inception in compressors: the modal inception (long-length scale) and the spike-type inception (short-length scale). The modal inception (long-length scale) has been extensively studied and is believed to be well understood [3,4]; its inception can be successfully described without considering details of the flow inside the blade passages. On the other hand, the spike-type inception (short-length scale) is not fully understood yet, especially in high-speed compressors and, because the spike disturbances are comparable in scale to the mean velocity through the compressor, its analysis requires the understanding of the detailed flow structures inside the blade passage.

Recently, many studies have been reported on the role of flow structure in spike-type stall inception in low-speed compressors [5–7]. Their study indicates that there are two main criteria behind the stall inception: the net upstream mass flow at the trailing edge of the blade tip and the leading-edge tip clearance flow spillage. But the flow mechanism behind the stall inception is not as well understood in high-speed compressors as it is in low-speed compressors. Few experimental or analytical studies have been reported on stall inception in a high-speed compressor.

He and Ismael [8] numerically simulated stall inception in an isolated compressor blade row. Their study indicates that an isolated blade row with supersonic inflow tends to stall in a one-dimensional surgelike pattern without first experiencing stall. Niazi et al. [9] numerically simulated stall inception in an isolated transonic

Presented as Paper 2009-5374 at the 45th AIAA/ASME/SAE/ASEE Joint Propulsion Conference and Exhibit, Denver, CO., 1 August 2009; received 5 April 2010; revision received 15 July 2010; accepted for publication 10 August 2010.

*Postdoctoral Fellow, School of Aerospace Engineering. Member AIAA.
†Regents Professor and Associate Chair (Academic), School of Aerospace Engineering. Associate Fellow AIAA.
‡Professor, School of Aerospace Engineering. Associate Fellow AIAA.

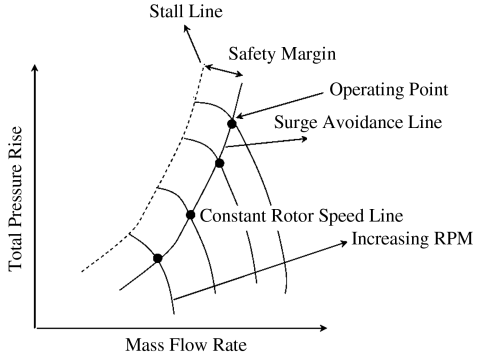

Fig. 1 Typical compressor characteristic map.

compressor blade row. Their study showed that at low mass flow rates, the tip leakage flow becomes stronger, and its interaction with the tip shock leads to compressor stall. Hah et al. [10] performed an unsteady Reynolds-averaged Navier–Stokes (RANS) analysis for an isolated transonic compressor rotor. The numerically produced signal, in terms of axial velocity, was very similar to the measured stall signals from high-response pressure transducers mounted upstream of the rotor. Their numerical analysis revealed that the axial positions of shocks detached from the rotor blades varies from blade to blade, and that this nonuniform shock front produces the stall signal. Haixin et al. [11] studied the stall mechanism in an isolated transonic axial compressor rotor with different tip gap heights. They found that for small-tip gaps (0.4% blade span), the burst up of the trailing-edge vortex will trigger the stall, while for large-tip gaps (1.0% blade span), the leading-edge blade-tip leakage vortex will trigger the stall instead. Chima [12] developed and used a three-dimensional unsteady Euler computational fluid dynamics (CFD) code to investigate compressor stall and stability. In his investigations on NASA stage 35, he found that both radial and circumferential distortions reduced the stable flow range of the compressor. Hah et al. [13] carried out computational simulations to identify the flow mechanisms behind the spike-type stall inception in a transonic compressor rotor. They found that the unsteady random behavior of the tip clearance vortex and its interactions with the passage shock seemed to be critical ingredients in the development of spike-type stall in a transonic compressor. They showed that the spike-type stall develops after the passage shock is fully detached from the blade passages and, as the stalled blade passages are formed behind the passage shock, the stalled area rotates counter to the blade rotation, just like the classical Emmons-type rotating stall.

III. Research Objectives

Most of the studies that have been done to date used a RANS solver coupled with either a one- or two-equation turbulence model. Reference [14] gives an excellent review of turbulence models available in commercial CFD codes through the analysis of a range of turbomachinery applications.

Because of the complicated physics behind stall inception, turbulence modeling plays a very important role in its detection. Thus, there is a huge need for more sophisticated turbulence models, like detached-eddy simulation (DES) and hybrid RANS/large-eddy simulation (HRLES), where those models showed much better predictions compared with the regular two-equation turbulence models for a wide range of aerodynamic applications [15–18].

All of the aforementioned DES and HRLES approaches used a one-equation model in the free shear layers to estimate the velocity scales associated with turbulent eddies; the length scale was estimated based on grid spacing, as done in early large-eddy simulation (LES) work. Therefore, the transition between RANS and LES regions may depend entirely on the grid spacing, and it is not correlated with the local flow properties. To overcome this limitation, a hybrid RANS/kinetic-eddy simulation (HRKES) turbulence model has been developed by Zaki et al. [19] and Zaki [20]. The HRKES model solves Menter's k-ω-SST (shear stress transport) [21] model near walls and switches to the kinetic-eddy simulation (KES) model by Fang and Menon [22,23] away from walls. KES is a two-equation subgrid model for the LES of wall-bounded turbulent flow at high Reynolds numbers. This approach solves for both subgrid kinetic energy k and subgrid length scales l. The KES [22,23] model has been applied to static stall around a NACA0015 wing, oscillatory attached and dynamic light stall, and dynamic deep stall flows around a NACA0015 airfoil with good agreement with the experimental data. Thus, in the HRKES model, solving the k-ω-SST model near walls and the KES model away from walls alleviates the grid spacing dependency found in other DES and HRLES models. The HRKES [19,20] model has been applied to flows over different airfoil configurations (RAE2822 and NACA0015), a turbine vane configuration, and a compressor configuration, and it has been compared with the classical k-ω-SST turbulence model in [19,20]. It was found that blending k-ω-SST with KES using Menter's F_2 function showed much better predictions in separated flows than the baseline k-ω-SST model.

The objective of the current study is to carry out a numerical simulation of the stall inception in a transonic compressor stage (NASA stage 35), using the HRKES turbulence model and its ability to detect the stall onset. Then, the flowfield will be studied to understand the relevant flow mechanisms behind stall inception in the current case. In the following section, the HRKES turbulence model equations are described. Then, the present methodology is described.

IV. Hybrid Reynolds-Averaged Navier–Stokes/ Kinetic-Eddy Simulation Turbulence Model Formulation

This section presents the blended k-ω-SST/KES model equations. In the region close to the wall, Menter's k-ω-SST equations [21] are solved. The present HRKES turbulent kinetic energy equation is formulated as follows:

$$\frac{\mathrm{D}(\rho k)}{\mathrm{D}t} = \tau_{ij}\frac{\partial u_i}{\partial x_j} - \frac{k^{\frac{3}{2}}}{l} + \frac{\partial}{\partial x_j}\left[\left(\mu + \frac{\mu_t}{\sigma_k}\right)\frac{\partial k}{\partial x_j}\right] \tag{1}$$

The k-ω-SST model ω equation [21] is

$$\frac{\mathrm{D}(\rho\omega)}{\mathrm{D}t} = \frac{\gamma}{\upsilon_t}\tau_{ij}\frac{\partial u_i}{\partial x_j} - \beta\rho\omega^2 + \frac{\partial}{\partial x_j}\left[\left(\mu + \frac{\mu_t}{\sigma_\omega}\right)\frac{\partial \omega}{\partial x_j}\right] + 2.(1 - F_1)\rho\sigma_{\omega_2}\frac{1}{\omega}\frac{\partial k}{\partial x_j}\frac{\partial \omega}{\partial x_j} \tag{2}$$

In the outer region, the k equation is solved as before, and the ω equation is replaced by the kl equation from the KES model [22,23] as follows:

$$\frac{\mathrm{D}[\rho(kl)]}{\mathrm{D}t} = C_l l\tau_{ij}\frac{\partial u_i}{\partial x_j} - C_{kl}\rho k^{\frac{3}{2}} + \frac{\partial}{\partial x_j}\left[\left(\mu + \frac{\mu_t}{\sigma_{kl}}\right)\frac{\partial (kl)}{\partial x_j}\right] \tag{3}$$

To avoid abrupt jumps in the values of l between near-wall regions and the outer layer, the following blending is used in computing the HRKES length scale:

$$l = F_{\text{blend}}.l_{k\text{-}\omega\text{-SST}} + (1 - F_{\text{blend}}).l_{\text{KES}}, \qquad l_{k\text{-}\omega\text{-SST}} = \frac{\sqrt{k}}{\beta^*\omega}$$
$$l_{\text{KES}} \rightarrow \text{computed from Eq. (3)} \tag{4}$$

Here, the shear stress term is computed from

$$\tau_{ij} = \mu_t\left(\frac{\partial u_i}{\partial x_j} + \frac{\partial u_j}{\partial x_i} - \frac{2}{3}\frac{\partial u_k}{\partial x_k}\delta_{ij}\right) - \frac{2}{3}\rho k\frac{\partial u_i}{\partial x_j} \tag{5}$$

The HRKES model constants are computed from k-ω-SST [21] and KES [22,23] model constants as follows:

$$\sigma_k = F_{\text{blend}}.[\sigma_{k_1}.F_1 + \sigma_{k_2}.(1-F_1)] + (1-F_{\text{blend}}).\sigma_{k_3}$$
$$\sigma_\omega = \sigma_{\omega_1}.F_1 + \sigma_{\omega_2}.(1-F_1), \qquad \beta = \beta.F_1 + \beta.(1-F_1)$$
$$\gamma = \gamma_1.F_1 + \gamma_2.(1-F_1) \tag{6}$$

where

$$\sigma_{k_1} = 1/0.85, \quad \sigma_{\omega_1} = 2.0, \quad \beta_1 = 0.075, \quad \beta^* = 0.09$$
$$\sigma_{k_2} = 1.0, \quad \sigma_{\omega_2} = 1/0.856, \quad \beta_2 = 0.0828$$
$$\sigma_{k_3} = 0.9, \quad \sigma_{kl} = 2.0, \quad C_l = 1.06, \quad \kappa = 0.41$$
$$\gamma_1 = \frac{\beta_1}{\beta^*} - \frac{\kappa^2}{\sigma_{\omega_1}\sqrt{\beta^*}}, \qquad \gamma_2 = \frac{\beta_2}{\beta^*} - \frac{\kappa^2}{\sigma_{\omega_2}\sqrt{\beta^*}} \tag{7}$$

The function F_1 is calculated from

$$F_1 = \tanh\left(\left(\min\left[\max\left[\frac{2\sqrt{k}}{\beta^*\omega y}; \frac{500\nu}{y^2\omega}\right]; \frac{4\rho\sigma_{\omega_2}k}{CD_{k\omega}y^2}\right]\right)^4\right)$$
$$CD_{k\omega} = \max\left[2\rho\sigma_{\omega_2}\frac{1}{\omega}\frac{\partial k}{\partial x_j}\frac{\partial \omega}{\partial x_j}; 10^{-20}\right] \tag{8}$$

The dissipation coefficient of the kl equation is computed as a function of length scale gradients [23] as follows:

$$C_{kl} = 0.58 + 2\frac{C_\upsilon}{\sigma_{kl}}\left(\frac{\partial l}{\partial x_j}\right)^2 \tag{9}$$

Where C_υ is computed following the realizability constraints [23]. Its value has a lower bound that is based on the ratio of the turbulent time scale ($t = l/\sqrt{k}$) to the shear time scale ($t = 1/\sqrt{(S_{ij}S_{ij} - \frac{1}{3}S_{kk}^2)}$) as follows:

$$C_\upsilon = \min\left[0.0667; \frac{1}{\sqrt{6}}\frac{(\sqrt{k}/l)}{\sqrt{S_{ij}S_{ij} - (1/3)S_{kk}^2}}\right] \tag{10}$$

Finally, the turbulent viscosity is computed from

$$\mu_t = F_{\text{blend}}\mu_t|_{k\text{-}\omega\text{-SST}} + (1-F_{\text{blend}})\mu_t|_{\text{KES}}$$
$$\mu_t|_{k\text{-}\omega\text{-SST}} = \frac{0.31\rho k}{\max(0.31\omega; \Omega F_2)}$$
$$\mu_t|_{\text{KES}} = C_\upsilon \rho\sqrt{k} l_{\text{KES}} \tag{11}$$

Where the function F_2 is computed as follows:

$$F_2 = \tanh\left(\left(\max\left[\frac{2\sqrt{k}}{\beta^*\omega y}; \frac{500\nu}{y^2\omega}\right]\right)^2\right) \tag{12}$$

The blending function options found in the current HRKES model are Menter's k-ω-SST [21] F_1 and F_2 functions. Those distance-dependent blending functions were chosen to insure a smooth transition between the RANS model in near-wall regions and the LES model away from walls. Four different options for the HRKES model (a combination of F_1 and F_2 blending functions and the use of realizability constraints to bound the KES model parameters) have been coded, studied, and compared with the classical k-ω-SST turbulence model in previous studies by Zaki et al. [19] and Zaki [20]. As mentioned in the previous section, it was found that blending k-ω-SST with KES using the k-ω-SST F_2 function showed better predictions in separated flows than the k-ω-SST model. Hence, the F_2 blending function is used in the current HRKES model. For more details about the HRKES turbulence model, boundary conditions, and initial conditions, the reader is referred to [19,20].

V. Current Methodology

The present studies were done using an in-house solver GT-TURBO3D (Georgia Tech Turbomachinery 3D) [24–28]. This solver is a spatially high-order unsteady three-dimensional compressible flow solver that uses an implicit time marching scheme and a two-equation k-ω-SST turbulence model. This solver has been extensively validated for helicopter rotors, wind turbines, prop fans, fixed-wing configurations, and single-stage axial and radial compressors [24–27]. As a further validation of this analysis, this solver was also evaluated by Zaki et al. [28] for different single and multistage axial turbine configurations. The Hybrid RANS/KES turbulence model has been developed, implemented, evaluated, and studied for flows over a different airfoil configurations (RAE2822 and NACA0015), a turbine vane configuration, and a compressor configuration by Zaki et al. [19] and Zaki [20]. The code structure, validation, and grid convergence studies are documented in the aforementioned references and are not reproduced here for brevity.

VI. Results and Discussions

In this section, the present methodology is applied to study the flow mechanism behind stall inception in the NASA stage 35 compressor configuration as a representative of a modern compressor stage. NASA stage 35 is a transonic inlet stage for a core compressor (a rotor followed by a stator), and it has been widely used by several researchers. This stage was originally designed and tested at NASA John H. Glenn Research Center by Reid and Moore [29]. This compressor stage has a design pressure ratio of 1.82 at a mass flow rate of 20.19 kg/s, and it has a rotor-tip speed of 455 m/s. The rotor has 36 multiple-circular-arc blades with a maximum radius of 9.94 cm, a hub-to-tip ratio of 0.7, an aspect ratio of 1.19, and a tip solidity of 1.288. The stator has 46 multiple-circular-arc blades, with an aspect ratio of 1.26.

The grid used in the current work is shown in Fig. 2. It is a two-block (rotor block and stator block) H grid with 180 cells in the axial, 49 cell in the radial, and 54 cells in the azimuthal direction. At the rotor–stator interface, unsteady sliding mesh boundary conditions are used in the current analysis. Figure 3 shows the entropy contours at the midspan of the compressor stage. It is seen that the rotor wake is preserved across the rotor–stator interface with a slight dissipation due to the interpolation between the two sides of the interface boundary. The rotor wake skewing and stretching while passing through the stator blade passage can also be seen in this Fig. 3.

To study the flow structure at near-stall conditions, the flowfields along a compressor speed line are simulated. A single blade passage is modeled here, assuming blade passage to blade passage periodicity. Although full annulus analysis is needed to simulate the compressor rotating stall inception, similar flow phenomena can occur in a single blade passage during actual rotating stall inception [30] while requiring much lower computational resources. This assumption is considered adequate up to the stall inception point [31]. The simulations presented here are carried out using both the baseline k-ω-SST turbulence model and the HRKES turbulence model.

Figure 4 shows the compressor stage computed and measured [29] characteristics at the design rotational speed, using both the k-ω-SST and HRKES turbulence models. On the vertical axis, the total pressure ratio rise across the compressor stage is plotted against the normalized mass flow rate ($\dot{m}/\dot{m}_{\text{choked}}$) on the horizontal axis and compared with the experimental [29] data. The compressor stage characteristics are generated here by running different simulations to different static backpressures. First, the near-choke condition, flow points are run to low-static backpressure values, and then the solutions are restarted with incrementally increasing the static backpressure to compute the intermediate points on the speed line toward stall. Since the current simulations are unsteady, time-averaged solutions are obtained by averaging over multiple cycles after the cyclic convergence is achieved. Examining Fig. 4, the computational results and the computed characteristic line shape agree well with the experimental [29] results for both the k-ω-SST and HRKES turbulence models. However, the HRKES model was found superior

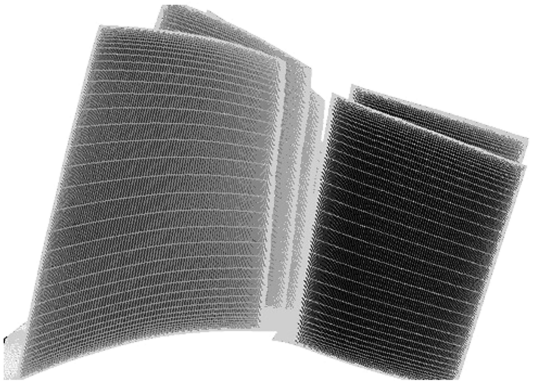

a) Compressor stage grid overview

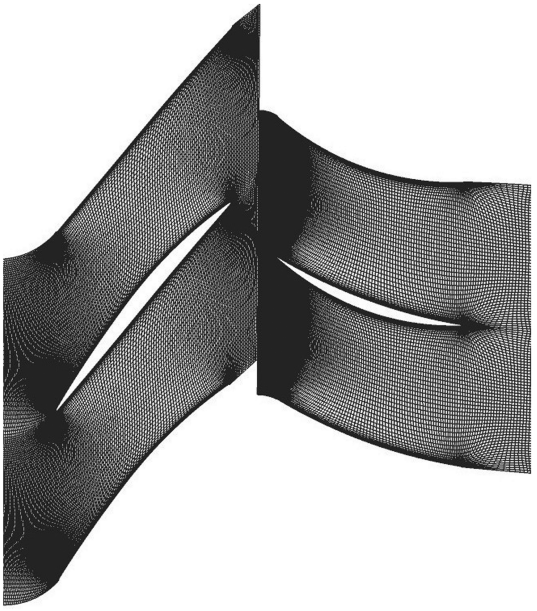

b) Blade-to-blade grid at midspan

Fig. 2 Two block (180 × 49 × 54) H grid for the NASA stage 35.

to the k-ω-SST model in predicting the stall inception. For the HRKES model simulations, point A represents the near-design operating condition, point B represents the near-stall operating condition, and point C is in stall condition. Increasing the static backpressure after point B for the HRKES model simulations causes the compressor to stall, while the k-ω-SST model simulations do not capture the compressor stall for the same static backpressure conditions. Other 2-D studies by Zaki et al. [19] and Zaki [20] have also shown that the HRKES model distinguishes itself in predicting stall and poststall behavior.

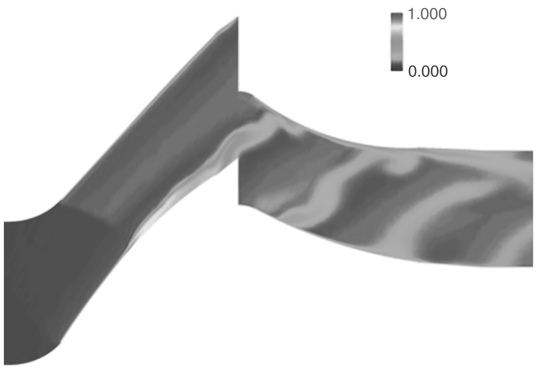

Fig. 3 Nondimensional entropy contours for the NASA stage 35.

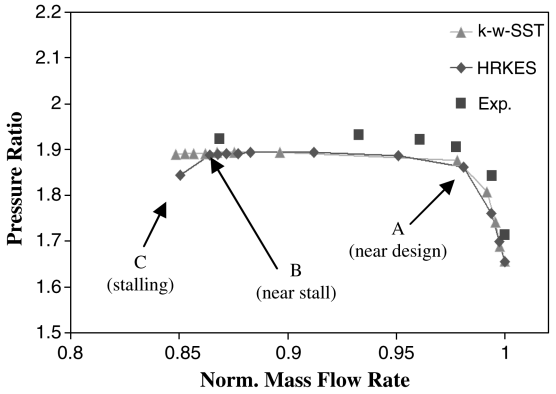

Fig. 4 NASA stage 35 compressor speed line.

As mentioned earlier, the main objective behind this work is to explore the flow mechanisms and the physical trends leading to the stall inception in the current compressor configuration as a representative of a modern compressor stage. Since earlier experimental investigations (Suder et al. [32]) and numerical studies (Chen et al. [33]) indicated that stall initiates in the tip region of the rotor for this compressor stage configuration, the flowfields in the rotor-tip region at the two operating points A and B along the compressor speed line, shown in Fig. 4, are studied in detail to examine the role of the tip clearance flow and the shock wave as the compressor marches toward stall. Although the current simulations are carried out using the k-ω-SST and the HRKES turbulence models, only the simulations obtained using the HRKES model will be analyzed here, given the superior behavior of HRKES compared with k-ω-SST, as shown previously. The results presented in the current work are obtained from single passage simulations and duplicated over two neighboring blade passages for better visualization.

Figure 5 shows the nondimensional static pressure contours, which are independent of the frame of reference, at the tip section of the rotor blade, on the casing walls, and at corresponding stator span sections for both operating points A and B. Because of the transonic nature of the flow, supersonic flow appears when the rotor rotational velocity is combined with the main flow axial velocity and the relative Mach number exceeds unity, which leads to the formation of shock waves. Tip vortices and tip clearance leakage flow are generated in the flow due to the pressure difference between the pressure side and the suction side of the rotor blade in a similar manner to the formation of the aircraft wingtip vortices. High-pressure flow from the blade's pressure surface rolls over the blade tip to reach the lower-pressure flow over the blade's suction surface. The lower axial momentum rotor-tip leakage flow interacts with the main axial flow, creating a vortex sheet that rolls up into the leakage vortex as it travels downstream. The formation of the tip leakage flow vortex reduces the effective main flow stream area and adds more blockage to the flow passage. As the mass flow rate through the compressor decreases, the angle of the tip vortex will increase, impinging at a more forward location on the adjacent rotor blade surface. This can cause the flow to spill over the adjacent blade leading edge and induce stall [7,34].

As the compressor marches toward stall, from point A to point B, the following flow phenomena are identified. In Fig. 5, darker regions represent low-pressure areas, and lightly shaded regions correspond to high-pressure areas. In Fig. 5a, for the near-design operating point A, the low-pressure area (very dark) extending from the rotor tip to midpassage represents the tip clearance leakage flow vortex as it travels downstream. Looking at the shock wave, it is observed that the shock wave is very close to the rotor leading edge, and the shock front is uniform. The shock wave passes continuously across the passage, where it intersects with the tip vortex and bends. The shock wave then continues until it intersects the rotor suction surface. In Fig. 5b, for the near-stall operating point B, the low-pressure area (very dark) near the rotor tip represents the tip clearance leakage flow vortex as it travels downstream. Looking at the shock wave, it is seen that the shock wave stands further upstream from the rotor leading edge compared with the near-design condition, and it becomes

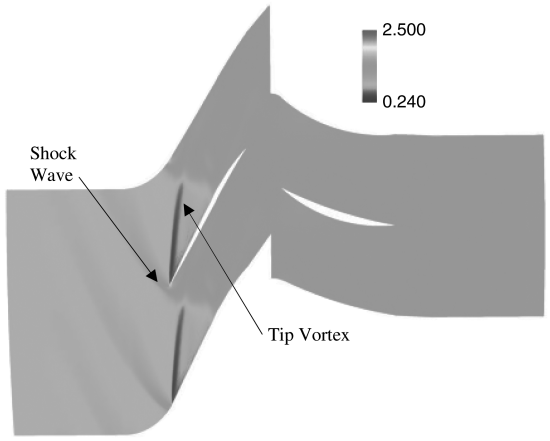

a) Operating point A

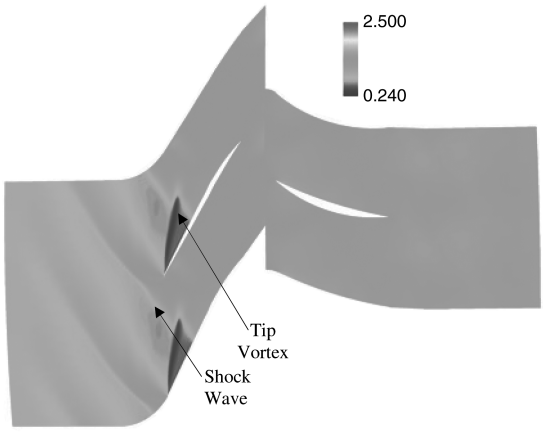

b) Operating point B

Fig. 5 Nondimensional static pressure contours at the tip section for NASA stage 35.

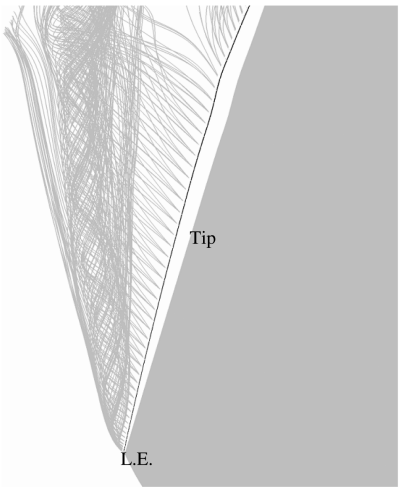

a) Operating point A

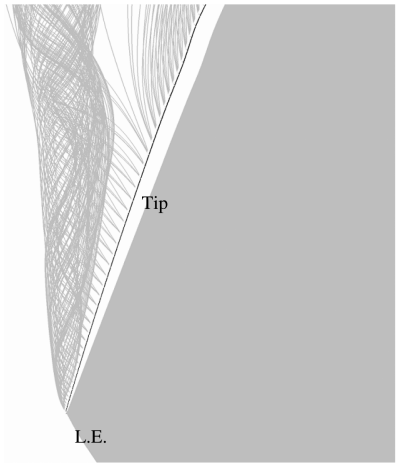

b) Operating point B

Fig. 6 NASA stage 35 rotor-tip leakage flow streamlines (L.E. denotes leading edge).

stronger. The shock wave front becomes nonuniform, which indicates the high unsteadiness of the shock wave at the near-stall condition. The shock wave passes continuously across the passage, where it intersects with the tip vortex closer to the rotor blade suction surface compared with the near-design condition. The shock wave then bends before intersecting the rotor suction surface further upstream compared with the near-design condition. Similar flow structures to that in Fig. 5 are seen on the casing.

Figure 6 shows the rotor-tip clearance flow streamlines for the two operating points A and B. By looking at the rotor-tip clearance flow streamlines for the near-design operating point A in Fig. 6a, it is observed that only the forward 20% of the tip leakage flow emerges to form the tip leakage flow vortex core. The vortex interacts with the shock wave near the midpassage plane. The interaction between the shock wave and the tip vortex is not strong, and it slightly alters the shape and trajectory of the vortex. In Fig. 6b, for the near-stall operating point B, it is again seen that only the forward 20% of the tip leakage flow emerges to form the tip leakage flow vortex core, which is now moved further forward compared with the near-design condition. Because of the high blade loading at near-stall condition, which means a larger pressure difference between the pressure surface and the suction surface of the rotor blade near the tip, the tip vortex is larger in size compared with the near-design condition. The vortex interacts with the shock wave closer to the rotor suction surface. The interaction between the shock wave and the tip vortex is strong, and it impacts the shape and trajectory of the vortex. The center portion of the vortex now becomes perpendicular to the axial flow direction. This trend agrees well with the stall inception criterion of Hoying et al. [34]. In their work, Hoying et al. [34] developed a criterion for stall inception, using vortex kinematics analysis, when the trajectory of the tip clearance vortex becomes perpendicular to the axial flow direction.

Figures 7 and 8 show the flowfield entropy contours in the blade-to-blade midpassage plane and at the rotor blade leading-edge plane, respectively, for the near-design operating point A and the near-stall operating point B. In those figures, darker regions represent low-entropy areas, and lightly shaded regions correspond to high-entropy areas. Entropy rises in the tip vortex, and this can be observed clearly. In Fig. 7a, for the near-design condition, it can be seen that the shock wave interactions with the tip vortex are not strong. In Fig. 7b, for the near-stall condition, it is seen that the rotor blade-tip vortex is larger in size, and its interactions with the shock wave are stronger at near stall compared with the near-design condition. Figure 7 also shows the entropy rise across the rotor blade passage at the tip at the near-stall condition, which was also indicated by Chima [12] for this compressor configuration. Examining the rotor leading-edge plane (Fig. 8), it is found that the entropy increases at the near-stall condition as compared with the near-design conditions. This low-momentum flow region near the rotor blade-tip leading edge will cause the flow spillage over it.

Furthermore, when a shock wave interacts with a boundary layer, the low-momentum flow in the boundary layer is subjected to the pressure rise across the shock wave. This sudden pressure rise acts as a high adverse pressure gradient on the boundary layer and, if the shock wave is strong enough, the pressure rise across it will cause the boundary layer to separate. Therefore, the possibility of the shock boundary-layer interactions to induce flow separation is investigated. In the rotor blade passage, this can only occur in two locations where

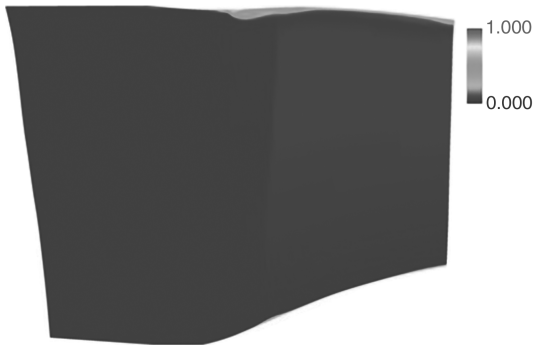

a) Operating point A

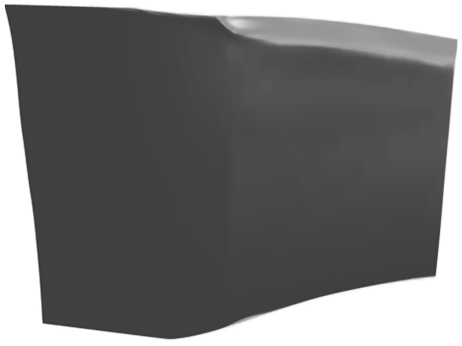

b) Operating point B

Fig. 7 Nondimensional entropy contours at the NASA stage 35 rotor midpassage.

the shock wave interacts with the tip clearance leakage flow vortex and with the boundary layer over the casing surface. The first location is over the rotor-tip suction surface and, by examining the rotor-tip clearance flow streamlines at the near-stall condition shown in Fig. 6b, it is seen that there is no flow separation in this region. The second location is on the casing surface. By examining the velocity vectors near the rotor blade casing in the blade-to-blade midpassage plane for the near-stall operating point B, as shown in Fig. 9, it is seen that the only reversed flow near the casing walls is the tip clearance vortex reversed flow, and there is no evidence of the casing flow separation in this case.

Finally, looking at the velocity vectors near the rotor blade-tip leading edge for the stalling point C, as shown in Fig. 10, flow spillage over the rotor-tip leading edge is observed, which follows well with the stall inception criterion of Vo et al. [7]. In their work, Vo et al. [7] showed that the stall inception is most likely accompanied by the forward spillage of the tip clearance vortex flow, which is seen here.

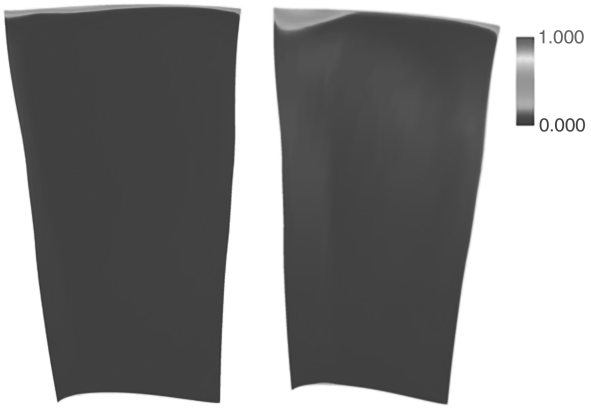

a) Operating point A b) Operating point B

Fig. 8 Nondimensional entropy contours at the NASA stage 35 rotor leading-edge planes.

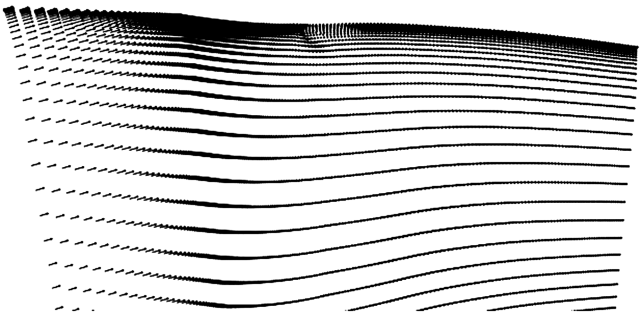

Fig. 9 Velocity vectors at the NASA stage 35 rotor midpassage plane at near-stall condition.

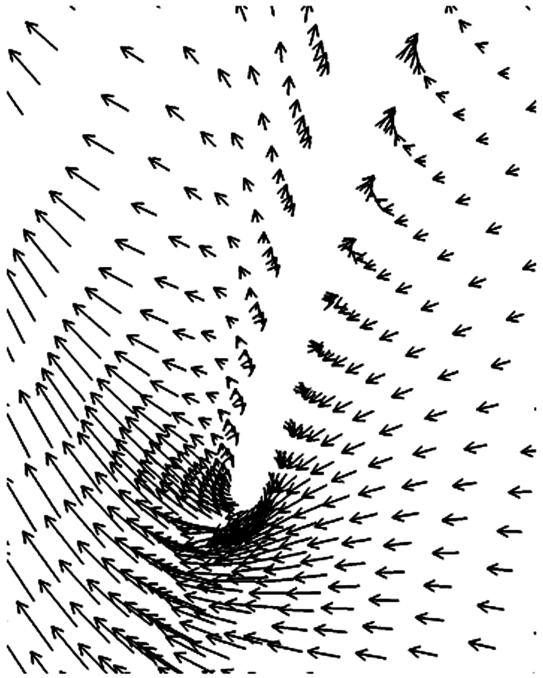

Fig. 10 Velocity vectors near the NASA stage 35 rotor-tip leading edge at stalling condition.

VII. Conclusions

The k-ω-SST and a HRKES turbulence models are used for the performance map predictions of the NASA stage 35 transonic axial compressor configuration. Both models (k-ω-SST and HRKES) gave satisfactory predictions of the performance map compared with the experimental data. However, the HRKES model was found superior to the k-ω-SST model in predicting the stall inception. For this reason, it is concluded that the HRKES is a more appropriate model for modeling compressor stall phenomena.

By studying the flowfields in the rotor-tip region at two operating points (near-design operating condition and near-stall operating condition), it is observed that at near stall, the shock wave is stronger and further upstream of the rotor leading edge compared with the near-design conditions. The tip vortex is larger in size due to the increased blade loading and is moved further forward. The interactions between the shock wave and the tip clearance leakage flow are stronger and alter the trajectory of the tip vortex, and the vortex trajectory becomes perpendicular to the main axial flow direction. Those interactions generate a low-momentum area near the adjacent rotor blade-tip leading edge, which will cause the flow spillage over it and lead to the stall inception in this compressor configuration.

References

[1] Gravdahl, J. T., and Egeland, O., *Compressor Surge and Rotating Stall: Modeling and Control*, Springer–Verlag, London, 1999.

[2] Emmons, H. W., Pearson, C. E., and Grant, H. P., "Compressor Surge and Stall Propagation," *Transactions of the ASME*, Vol. 77, 1955, pp. 455–469.

[3] Moore, F. K., and Greitzer, E. M., "A Theory of Post-Stall Transients in Axial Compression Systems: Part 1, Development Equations," *Journal of Engineering for Gas Turbines and Power*, Vol. 108, No. 1, 1986, pp. 68–76.
doi:10.1115/1.3239887

[4] Moore, F. K., and Greitzer, E. M., "A Theory of Post-Stall Transients in Axial Compression Systems: Part 2, Application," *Journal of Engineering for Gas Turbines and Power*, Vol. 108, No. 2, 1986, pp. 231–239.
doi:10.1115/1.3239893

[5] Camp, T. R., and Day, I. J., "A Study of Spike and Modal Stall Phenomena in a Low-Speed Axial Compressor," *Journal of Turbomachinery*, Vol. 120, No. 3, 1998, pp. 393–401.

[6] Gong, Y., Tan, C. S., Gordon, K. A., and Greitzer, E. M., "A Computational Model for Short Wavelength Stall Inception and Development in Multi-Stage Compressors," *Journal of Turbomachinery*, Vol. 121, No. 4, 1999, pp. 726–734.
doi:10.1115/1.2836726

[7] Vo, H. D., Tan, C. S., and Greitzer, E. M., "Criteria for Spike Initiated Rotating Stall," American Society of Mechanical Engineers Paper GT2005-68374, Fairfield, NJ, 2005.

[8] He, L., and Ismael, J. O., "Computations of Blade Row Stall Inception in Transonic Flows," *The Aeronautical Journal*, Vol. 103, No. 1025, July 1999, pp. 317–324.

[9] Niazi, S., Stein, A., and Sankar, L. N., "Numerical Study of Surge and Stall Alleviation in a High-Speed Transonic Fan Rotor," AIAA Paper 2000-0225, 2000.

[10] Hah, C., Rabe, D. C., and Wadia, A. R., "Role of Tip-Leakage Vortices and Passage Shock in Stall Inception in a Swept Transonic Compressor Rotor," American Society of Mechanical Engineers Paper GT2004-53867, Fairfield, NJ, 2004.

[11] Haixin, C., Xudong, H., and Song, F., "CFD Investigation on Stall Mechanism and Casing Treatment of a Transonic Compressor," 42nd AIAA/ASME/SAE/ASEE Joint Propulsion Conference and Exhibit, AIAA Paper 2006-4799, July 2006.

[12] Chima, R. V., "A Three-Dimensional Unsteady CFD Model of Compressor Stability," *Proceedings of GT2006*, American Society of Mechanical Engineers Paper GT2006-90040, Fairfield, NJ, 2006.

[13] Hah, C., Bergner, J., and Schiffer, H. P., "Short Length-Scale rotating Stall Inception in a transonic axial Compressor: CRITERIA and Mechanism," *Proceedings of GT2006*, American Society of Mechanical Engineers, Paper GT2006-90045, Fairfield, NJ, 2006.

[14] Beevers, A., Ivey, P., Amaral-Teixeira, J. A., and Wells, R., "A Review of Turbulence Models Available in a Commercial CFD Code through the Analysis of a Range of Turbomachinery Applications," *Proceedings of GT2007*, American Society of Mechanical Engineers, Paper GT2007-28053, Fairfield, NJ, 2007.

[15] Strelets, M., "Detached Eddy Simulation of Massively Separated Flows," 39th AIAA Aerospace Sciences Meeting and Exhibit, AIAA Paper 2001-0879, Jan. 2001.

[16] Kapadia, S., Roy, S., and Heidmann, J., "Detached Eddy Simulation of Turbine Blade Cooling," 36th AIAA Thermophysics Conference, AIAA Paper 2003-3632, June 2003.

[17] Li, D., Men'shov, I., and Nakamura, Y., "Detached-Eddy Simulation of Three Airfoils with Different Stall Onset Mechanisms," *Journal of Aircraft*, Vol. 43, No. 4, 2006, pp. 1014–1021.
doi:10.2514/1.17274

[18] Basu, D., Hamed, A., Das, K., and Tomko, K., "Comparative Analysis of Hybrid Turbulence Closure Models in the Unsteady Transonic Separated Flow Simulations," 44th AIAA Aerospace Sciences Meeting and Exhibit, AIAA Paper 2006-117, Jan. 2006.

[19] Zaki, M., Menon, S., and Sankar, L., "Hybrid Reynolds-Averaged Navier–Stokes and Kinetic Eddy Simulation of External and Internal Flows," *Journal of Aircraft*, Vol. 47, No. 3, May–June 2010, pp. 805–811.
doi:10.2514/1.43454

[20] Zaki, M., "Physics Based Modeling of Axial Compressor Stall," Ph.D. Dissertation, School of Aerospace Engineering, Georgia Inst. of Technology, Atlanta, GA, Dec. 2009.

[21] Menter, F. R., "Two-Equation Eddy-Viscosity Turbulence Models for Engineering Applications," *AIAA Journal*, Vol. 32, No. 8, 1994, pp. 1598–1605.
doi:10.2514/3.12149

[22] Fang, Y., and Menon, S., "A Two Equation Subgrid Model for Large Eddy Simulation of High Reynolds number Flows," 44th AIAA Aerospace Sciences Meeting and Exhibit, AIAA Paper 2006-116, Jan. 2006.

[23] Fang, Y., and Menon, S., "Kinetic Eddy Simulation of Static and Dynamic Stall," 24th Applied Aerodynamics Conference, AIAA Paper 2006-3847, June 2006.

[24] Stein, A., Niazi, S., and Sankar, L. N., "Computational Analysis of the Centrifugal Compressor Surge Control using Air Injection," *Journal of Aircraft*, Vol. 38, No. 3, May–June 2001, pp. 513–520.
doi:10.2514/2.2791

[25] Stein, A., Niazi, S., and Sankar, L. N., "Computational Analysis of Surge and Separation Control in Centrifugal Compressors," *Journal of Propulsion and Power*, Vol. 16, No. 1, Jan.–Feb. 2000, pp. 65–71.
doi:10.2514/2.5532

[26] Niazi, S., Stein, A., and Sankar, L. N., "Computational Analysis of Stall Control Using Bleed Valve in a High-Speed Compressor," 36th AIAA Joint Propulsion Conference, AIAA Paper 2000-3507, 2000.

[27] Niazi, S., Stein, A., and Sankar, L. N., "Numerical Studies of Stall and Surge Alleviation in a High-Speed Transonic Fan Rotor," 38th AIAA Aerospace Sciences Meeting, AIAA Paper 2000-0225, 2000.

[28] Zaki, M., Iyengar, V., and Sankar, L., "Assessment of Rotor-Stator Interface Boundary Condition Techniques for Modeling Axial Flow Turbines," 42nd AIAA/ASME/SAE/ASEE Joint Propulsion Conference and Exhibit, AIAA Paper 2006-4619, July 2006.

[29] Reid, L., and Moore, R. D., "Design and Overall Performance of Four Highly-Loaded, High-Speed Inlet Stages for an Advanced, High-Pressure-Ratio Core Compressor," NASA TP 1337, 1978.

[30] Hah, C., Bergner, J., and Schiffer, H. P., "Short Length-Scale Rotating Stall Inception in a Transonic Axial Compressor—Criteria and Mechanism," *Proceedings of GT2006*, American Society of Mechanical Engineers, Paper GT2006-90045, Fairfield, NJ, 2006.

[31] Davis, R. L., and Yao, J., "Prediction of Compressor Stage Performance from Choke Through Stall," 43rd AIAA Aerospace Sciences Meeting, AIAA Paper 2005-1005, 2005.

[32] Suder, K. L., Hathaway, M. D., Thorp, S. A., Strazisar, A. J., and Bright, M. M., "Compressor Stability Enhancement Using Discrete Tip Injection," *Journal of Turbomachinery*, Vol. 123, No. 1, 2001, pp. 14–23.
doi:10.1115/1.1330272

[33] Chen, J., Hathaway, M. D., and Herrick, G. P., "Pre-Stall Behavior of a Transonic Compressor Stage via Time Accurate Numerical Simulation," NASA TM 2008-215163, 2008.

[34] Hoying, D. A., Tan, C. S., Vo, H. D., and Greitzer, E. M., "Role of Blade Passage Flow Structures in Axial Compress Rotating Stall Inception," *Journal of Turbomachinery*, Vol. 121, No. 4, 1999, pp. 735–742.
doi:10.1115/1.2836727

J. Oefelein
Associate Editor